



OPEN

SUBJECT AREAS:
ENERGY TRANSFER
OPTICAL PROPERTIES AND
DEVICES

Covalent functionalization of graphene by azobenzene with molecular hydrogen bonds for long-term solar thermal storage

Yiyu Feng¹, Hongpo Liu¹, Wen Luo¹, Enzuo Liu¹, Naiqin Zhao¹, Katsumi Yoshino² & Wei Feng¹Received
29 August 2013Accepted
4 November 2013Published
19 November 2013Correspondence and
requests for materials
should be addressed to
W.F. (weifeng@tju.
edu.cn)¹School of Materials Science and Engineering, Tianjin Key Laboratory of Composite and Functional Materials, Tianjin University, Tianjin 300072, China, ²Shimane Institute for Industrial Technology, Hokuryo-cho, Mastue, Shimane 690-0816, Japan.

Reduced graphene oxide-azobenzene (RGO-AZO) hybrids were prepared via covalent functionalization for long-term solar thermal storage. Thermal barrier (ΔE_a) of *cis* to *tran* reversion and thermal storage (ΔH) were improved by molecular hydrogen bonds (H-bonds) through *ortho*- or *para*-substitution of AZO. Intramolecular H-bonds thermally stabilized *cis-ortho*-AZO on RGO with a long-term half-life of 5400 h ($\Delta E_a = 1.2$ eV), which was much longer than that of RGO-*para*-AZO (116 h). RGO-*para*-AZO with one intermolecular H-bond showed a high density of thermal storage up to 269.8 kJ kg⁻¹ compared with RGO-*ortho*-AZO (149.6 kJ kg⁻¹) with multiple intra- and intermolecular H-bonds of AZO according to relaxed stable structures. Thermal storage in experiment was the same order magnitude to theoretical data based on ΔH calculated by density functional theory and packing density. Photoactive RGO-AZO hybrid can be developed for high-performance solar thermal storage by optimizing molecular H-bonds.

Utilization of the sun as a renewable energy source based on the development of new materials and efficient devices is one of great challenges due to an increasing demand for energy impacts. Generally, an efficient and regenerative cycle is basically important for the use of solar energy including three steps – the capture of a great amount of photons, the conversion to useful form of energy, and reversible storage¹. Thus, numerous strategies to utilize sun's energy are presented such as photovoltaic, photo-catalysis, photo-synthesis and photo-thermalization, but few progresses on the conversion and storage of solar thermal energy have been made so far^{2–4}. Recently, photo-responsive metastable compounds are studied for close-cycle thermal storage because of their high potential capability of storage and reversible response. Such photo-responsive material stores a certain amount of solar energy in the chemical bonds through isomerization irradiated by solar light. By applying an external stimulus, the metastable moiety surmounts thermal barrier (ΔE_a for per molecule) and “releases” thermal energy (ΔH for per molecule). The material can be subsequently reused by the irradiation of light to induce isomerization and reversion for multiple cycles. This renewable material, which can be transportable in a liquid or power without the emission of chemicals to environment, is an ideal candidate for solar thermal storage.

Many photo-responsive molecules capable of undergoing photoisomerization are designed and prepared^{5,6}, but none achieves long-term and high-density storage. Azobenzene derivatives (AZO) show the great potential for solar thermal storage due to good absorption at 350–450 nm, reversible isomerization and thermal reversion controlled by functional groups and steric structures. However, the utilization of AZO is restricted by low density of thermal storage (ΔH for per molecule) during *cis* (Z) → *trans* (E) reversion, short half-lives ($\tau_{1/2}$, the time required for a quantity of Z-isomers to fall to half its value by Z → E reversion) of metastable states caused by low ΔE_a , and low work temperatures^{2,5,7–9}.

An important strategy to overcome these problems is to tune transition bands and the formation of molecular hydrogen bonds (H-bonds) in AZO by the incorporation of electron donating or withdrawing groups in the *ortho* position^{7–14}. Metastable Z-*ortho*-AZO is thermally stabilized by changing orbital energy or the formation of intramolecular H-bonds. Bléger et al. reported that Z-isomers of *ortho*-fluoro-AZO showed a long half-life of thermal reversion up to 714 days due to the separation of $n \rightarrow \pi^*$ transition bands¹¹, which provided a great promise for a long-term thermal storage. Recently, a carbon-based nanostructure attached to photo-responsive AZO molecules has been established for solar thermal storage^{13,14}. The calculation based on density functional theory (DFT) predicted that ΔE_a and ΔH for per AZO molecule on carbon nanotube (CNT) were controlled by molecular H-bonds. Compared with pure AZO, an increase in ΔH by more than two-times and high ΔE_a up to 1.25 eV ($\tau_{1/2}$ is longer than a year) were obtained for 2-2' hydroxyl-AZO with six H-bonds (four intramolecular



and two intermolecular H-bonds) in E-isomer and four H-bonds (two intramolecular and two intermolecular H-bonds) in Z-isomer¹³. On the basis of the interaction between AZO and carbon nanostructures, many studies reported on the control of isomerization and reversion of AZO bounded on graphene controlled by tuning the substitution of organic groups¹⁵. Isomerization of AZO tethered to graphene gives rise to the interaction between AZO and graphene¹⁶, which was also confirmed by the calculation based on DFT¹⁷. In spite of progresses on the calculation, the remarkable increase in both ΔH and ΔE_a for per AZO on graphene by optimizing inter and intramolecular H-bonds is still a great challenge because methods to improve the former often result in the decrease in the latter.

In this paper, two AZO molecules were covalently bound on reduced graphene oxides (RGO-AZO), and molecular H-bonds were controlled by the substitution (*ortho* or *para*) and close-packing arrays of AZO on RGO. Chemical structures, packing densities (the weight percentage of AZO for RGO-AZO) and the formation of H-bonds of AZO on RGO were studied by fourier transform infrared spectroscopy (FT-IR), proton nuclear magnetic resonance spectroscopy (NMR), X-ray photoelectron spectroscopy (XPS), and thermo gravimetric analysis (TGA). The effect of molecular H-bonds of AZO on ΔH and ΔE_a of RGO-AZO hybrids was investigated by isomerization and reversion using ultraviolet-visible (UV-vis) absorption spectra. The densities of thermal storage of RGO-AZO hybrids were experimentally measured by a microcalorimetric sensor and also calculated by DFT based on the relaxed stable structures.

Results

RGO was prepared by partial reduction of graphene oxide (GO) using NaBH_4 controlled by reaction time (1 h) and temperature (80°C). Two AZO chromophores, 4-sulfo-4'-amino-AZO (*para*-AZO) and 2-sulfo-2'-hydroxy-4'-amino-AZO (*ortho*-AZO, Figure S1) were covalently functionalized with RGO by the diazotization using diazonium salts^{18,19}. Figure 1 shows the synthesis route and chemical structures of RGO-*para*-AZO and RGO-*ortho*-AZO hybrids. Morphologies of RGO-AZO hybrids and RGO were observed by transmission electron microscopy (TEM). GO resembles crumpled silk veil with the clear boundary (Figure S2). RGO shows wrinkled nanosheets with slightly rough surfaces, and crystal lattices of RGO retains its hexagonal pattern after partial reduction according to corresponding fast fourier transforms (FTTs, inset of

Figure 2b). After the functionalization, the rough surface of dispersed nanosheets in Figure 2c and 2d appears to be covered by the addends, which form randomly distributed domains of immobilized AZO molecules²⁰. This microstructure is different from that of noncovalently functionalized graphene with organic molecules²¹. The domains affect the crystal lattices of the flakes in FTTs pattern (the inset of Figure 2d). Topological morphologies (Figure S3) are also found in RGO-AZO hybrid films. The compact structure favors the formation of molecular H-bonds among AZO molecules on the surface of nanosheets.

The covalent linkage between AZO and RGO was studied by FT-IR, NMR, and XPS spectra. As shown in Figure 3, C-N bands (brown circle) corresponding to (Ph) C-NH₂ at 1310 cm⁻¹ of *para*-AZO and at 1330 cm⁻¹ of *ortho*-AZO are disappeared in the spectra of RGO-*para*-AZO and RGO-*ortho*-AZO hybrids after the attachment. This feature is confirmed by N 1s XPS spectra (Figure S4), in which the N 1s regions of RGO-*para*-AZO and RGO-*ortho*-AZO hybrids show only one band of (Ph) N=N (Ph) at 400.1 eV²², and no peaks at 399.1 eV for (Ph) NH₂ are observed on the shoulder. Furthermore, the chemical shift (δ) at 5.39 corresponding to -NH₂ group in *ortho*-AZO is also not observed in RGO-*ortho*-AZO hybrids (not shown). Results indicate that AZO molecules are covalently attached on RGO rather than π -stacking. Intermolecular H-bonds of =S-OH---OH-S= between two adjacent AZO molecules on RGO were confirmed by red-shifted peaks of -SO₃H group on RGO-*ortho*-AZO and RGO-*para*-AZO hybrid in FT-IR spectra²³. The shifts of three characteristic peaks are clearly distinguished by dash lines in Figure 3. Red shifts by dozens of wavenumbers in sulfonic groups are observed in both RGO-*para*-AZO and RGO-*ortho*-AZO hybrids. RGO-*ortho*-AZO shows large red-shifts of two peaks of S-O vibration at 1180 and 1116 cm⁻¹ and one band of S-phenyl vibration at 1008 cm⁻¹ compared with *ortho*-AZO (1211, 1136 and 1018 cm⁻¹). Besides, red-shifted peaks are also observed in RGO-*para*-AZO (1164, 1110 and 1024 cm⁻¹) by comparison of *para*-AZO (1215, 1122 and 1037 cm⁻¹).

High packing density of AZO molecules on RGO is crucial for the control of closed arrays favoring the formation of intermolecular H-bonds between two adjacent molecules. The amounts of AZO functionalized on RGO were estimated by TGA (Figure 4a and 4b) and XPS spectra (Figure S5). RGO exhibits a good thermal stability and its weight loss is the elimination of remaining oxygen groups. The residual weight is 71.39%, 69.74%, and 67.63% at 700, 750, and

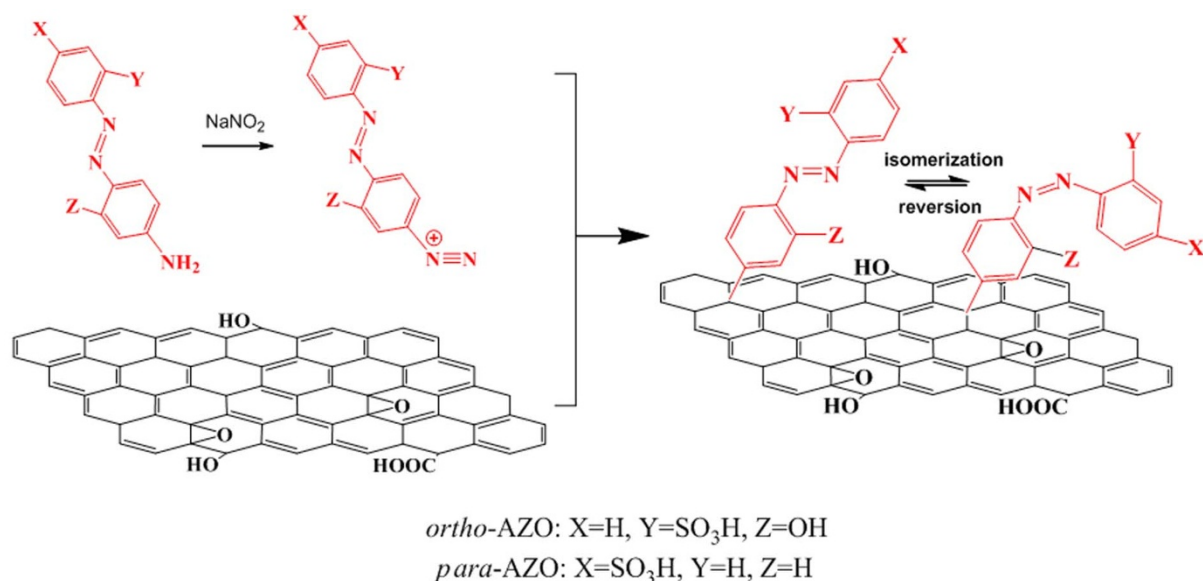


Figure 1 | The synthesis route and chemical structures of RGO-*para*-AZO and RGO-*ortho*-AZO hybrids by the diazotization.

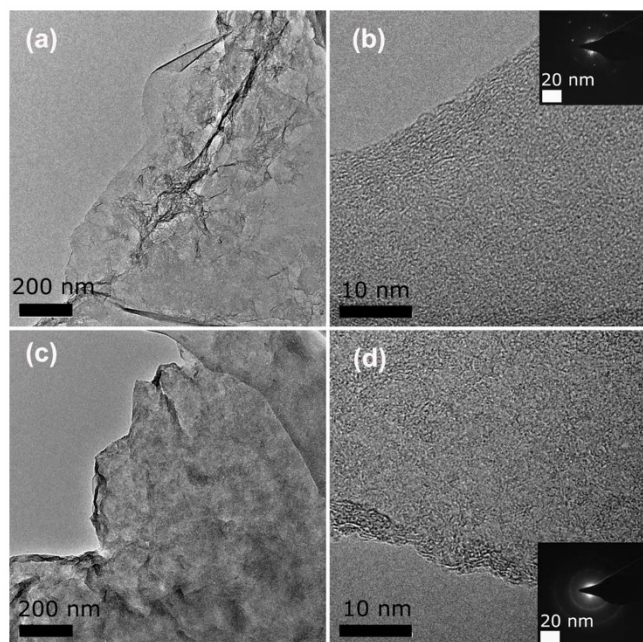


Figure 2 | TEM images of (a) RGO with high-resolution of (b) and the inset of FTTs pattern, (c) RGO-AZO hybrid with high resolution of (d) and the inset of FTTs pattern.

800°C. *Para*-AZO and *ortho*-AZO molecules are thermally stable from 30 to 220°C and subsequently show a sharp weight loss between ~220 and 370°C with a slow loss from 370 to 800°C. AZO molecules are almost completely combusted at 800°C. In Figure 4a and 4b, both

two RGO-AZO hybrids show weight loss properties because of the elimination of oxygen groups of RGO and the decomposition of AZO molecules with two stages. Thermal decomposition temperatures of two AZO molecules on RGO are slightly increased in comparison of AZO molecules.

On the basis of the distinctive weight loss of RGO and AZO, the packing density of AZO on RGO can be determined by residual weight percentages of RGO, AZO and RGO-AZO hybrids at three temperatures²⁴. As shown in Table S1, the weight percentages of AZO molecules on RGO-*para*-AZO are 59.5%, 60.4%, and 59.1% based on residue weights at 700, 750, and 800°C. Similarly, RGO-*ortho*-AZO hybrid shows the functionalization degree of AZO by 55.4%, 56.8%, and 58.2% at 700, 750, and 800°C. In addition, the degree was also estimated by element composition data in XPS²⁵. Based on the relative atomic percentage of sulphur and nitrogen in Table S2, weight percentages of *para*-AZO and *ortho*-AZO in hybrids are 61.14% and 63.78%, respectively. The average quantitative calculation based on TGA and XPS indicates that one AZO molecule is approximately covalently supported by per 11–12 carbon atoms of RGO by the diazotization^{18,25}. The densities confirmed by TGA and XPS pattern are much higher than that of AZO/graphene hybrid reported recently²⁶. The dense attachment favors the formation of intermolecular H-bonds of AZO on RGO¹³.

The interlayer effect and the crystallization of RGO-AZO hybrid are analyzed by XRD spectra (Figure 4c). The characteristic 2θ peak of GO at 11.5° corresponds to (0 0 1) interplanar spacing of 1.16 nm consistent with the thickness of GO in atomic force microscopy (AFM) images (Figure S2). RGO shows a broad band of (0 0 2) peak of graphite at $2\theta = 23.2^\circ$ corresponding to small d -spacing of 0.38 nm because of the aggregation of partially reduced sheets. The aggregation might arise from van der Waals interaction among

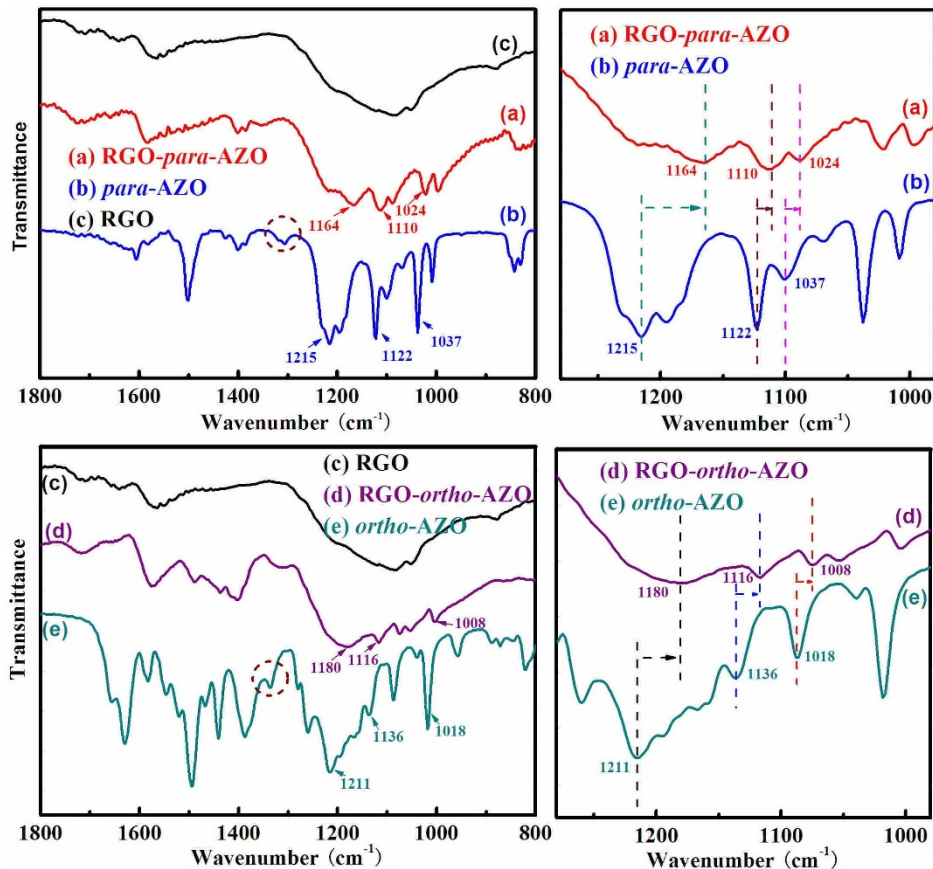


Figure 3 | FT-IR spectra of (a) RGO-*para*-AZO, (b) *para*-AZO, (c) RGO, (d) RGO-*ortho*-AZO and (e) *ortho*-AZO with the magnified view in the region of 1280–980 cm⁻¹. Arrows indicate the red-shifts of the bands corresponding to sulfonic group.

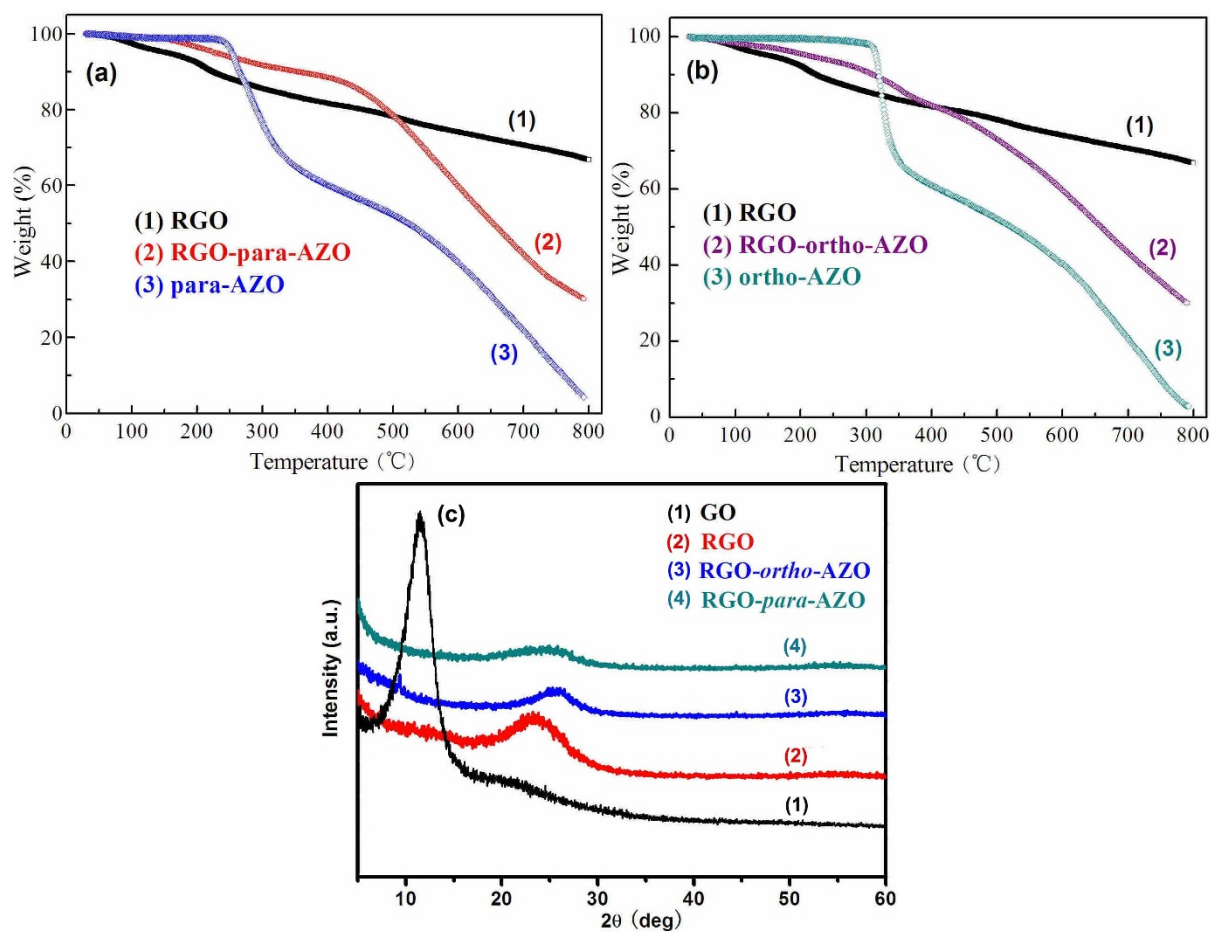


Figure 4 | TGA of (a) RGO, RGO-*para*-AZO and *para*-AZO, (b) RGO, RGO-*ortho*-AZO and *ortho*-AZO and (c) XRD patterns of GO, RGO, RGO-*ortho*-AZO and RGO-*para*-AZO.

nanosheets because the reduction weakens electrostatic repulsion. Therefore, the ultrasonication is necessary to disturb the stacking of nanosheets for well-dispersion of RGO before the functionalization with AZO molecules²⁷. The poor crystallization is found in RGO-AZO hybrids due to the thick organic layer attached on RGO. The weak peaks (0 0 2) of RGO-*para*-AZO and RGO-*ortho*-AZO with remarkably low intensity shifted to $2\theta = 24.8^\circ$ and 25.3° . This feature arises from stacked layers of sheets coated by non-crystalline AZO through the radical addition.

Discussion

Isomerization and thermal reversion of AZO are investigated by UV-vis absorption spectra. Time-evolved absorption spectra of RGO-*para*-AZO and RGO-*ortho*-AZO under the irradiation and after the irradiation in darkness were shown in Figure 5. Generally, one of strategies to optimize solar thermal storage is to maximize the absorption of sunlight. Compared with RGO-*para*-AZO at 344 nm, the maximum peak of E-*ortho*-AZO on RGO is 424 nm with a broad band with the edge up to 550 nm ascribed to π - π^* transition, indicating the control of isomerization by visible light^{8,10,11,28}. Photoisomerization of RGO-*para*-AZO (Figure 5a) and RGO-*ortho*-AZO (Figure 5c) hybrids is indicated by continuously decreased bands of *para*-AZO at 344 nm and *ortho*-AZO at 424 nm owing to the transformation from E- to Z-isomers. Electron transition in visible region and long-time isomerization (25 h until a photostationary equilibrium) indicate efficient absorption of high-energy solar power. This absorbed solar energy is basically important because it is required to be two-fold or three-fold higher than activation barrier

ΔE_i (energy required for isomerization of per AZO molecule)². According to previous studies, ΔH (energy stored by per AZO molecule) for per metastable Z-isomer must be less than ΔE_i in terms of equation (1), and the storage efficiency (the ratio of stored energy to absorbed solar energy) usually was <30% according to a review paper².

$$\Delta H = \Delta E_i - \Delta E_a \quad (1)$$

The kinetics and thermal barrier (ΔE_a for per Z-AZO molecule) were also studied. Thermal reversion of AZO with *ortho*- and *para*-substitution is observed in Figure S6. Compared with rapid reversion of *para*-AZO, Z-*ortho*-AZO is thermally stable with a long $\tau_{1/2}$ (the time required for a quantity of Z-AZO to fall to half its value by Z \rightarrow E reversion) of 116 hours at room temperature due to the formation of intramolecular H-bonds in Z-isomer (Figure S7). Thermal reversion of RGO-*para*-AZO (Figure 5b) and RGO-*ortho*-AZO (Figure 5d) in darkness is further studied by absorption spectra. After the functionalization, both two RGO-AZO hybrids show an appreciably slower thermal reversion of Z \rightarrow E isomerization with first-order rate constant several orders of magnitudes lower than that of AZO molecules (Figure 5e). An interesting result is found that RGO-*ortho*-AZO hybrid exhibits remarkable long-term thermal reversion of Z-isomers with a $\tau_{1/2}$ of 5400 hours (225 days), which is much longer than that (116 h) of RGO-*para*-AZO. The long $\tau_{1/2}$ indicates high ΔE_a for per metastable Z-AZO on RGO¹³. As shown in Table 1, ΔE_a for Z-*ortho*-AZO on RGO up to 1.2 eV calculated by equation (2) substantially outperforms other AZO derivatives^{5,7-10,29} and noticeably conquers the limitation of short reversion of Z-AZO.

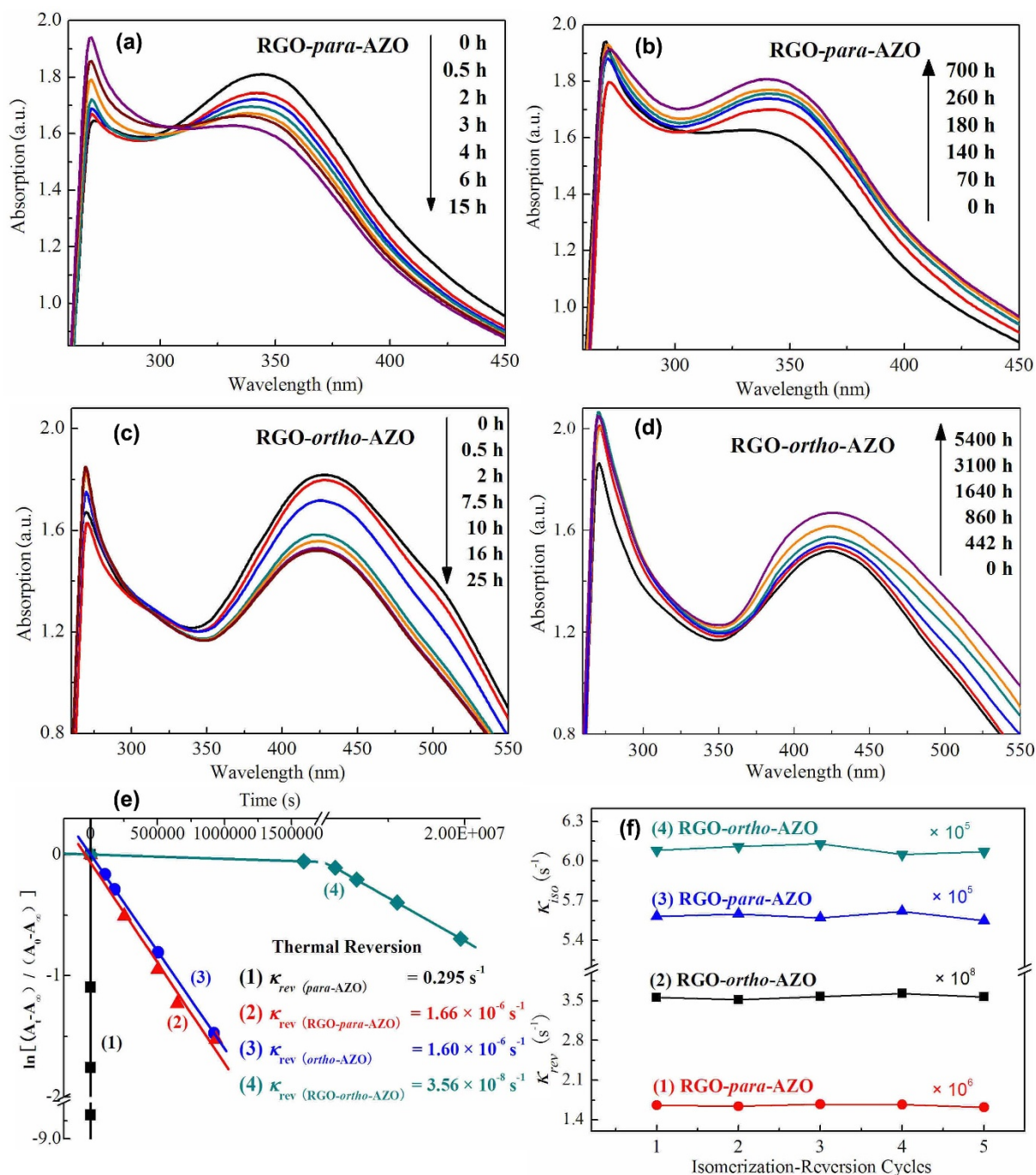


Figure 5 | Time-evolved absorption spectra of (a, b) RGO-*para*-AZO and (c, d) RGO-*ortho*-AZO hybrid under the irradiation of UV light at 365 nm and storage in darkness after the irradiation, and (e) First plots of $Z \rightarrow E$ thermal reversion of AZO and RGO-AZO hybrids with different κ_{rev} (the inset) and (f) κ_{rev} and κ_{iso} of RGO-*para*-AZO and RGO-*ortho*-AZO hybrids in five cycles.

$$\Delta E_a = -RT \ln \frac{h \ln 2}{\tau_{1/2} k_B T} \quad (2)$$

Where T is the storage temperature and $\tau_{1/2}$ is the half-life. k_B , R and h are the Boltzman, gas and Plank constants, respectively.

An important strategy to tune thermal reversion of AZO is the incorporation of electron-withdrawing or donating groups in the *ortho* position with molecular interaction^{7,10,11,13,30,31}. Intramolecular H-bonds in RGO-AZO hybrid are indicated by long-term reversion and large chemical shifts in ¹H NMR. According to previous calculation, the *di-ortho*-substitution (-OH) of Z-AZO on CNT resulted in a large increase in ΔE_a in Table 1 based on the stabilization of

Z-isomer by intramolecular H-bonds^{13,30}. Thus, compared with RGO-*para*-AZO showing no intramolecular H-bonds, high ΔE_a indicates the formation of intramolecular (=N---H-O) in *ortho*-AZO molecules on RGO. This analysis is supported by large chemical shifts (-O'H) of RGO-*ortho*-AZO at $\delta = 13.85$ in ¹H NMR^{32,33}, which is consistent with the chemical shift at (-O'H) $\delta = 14.19$ of *ortho*-AZO. Furthermore, RGO-AZO hybrids also show a good cycling stability of isomerization and thermal reversion, which follows first-order kinetics (equation S(1)). As shown in Figure 5f, first-order rate constants for reversion (κ_{rev}) of RGO-*ortho*-AZO and RGO-*para*-AZO only fluctuate in the range of $3.52\text{--}3.63 \times 10^{-8} \text{ s}^{-1}$ and $1.64\text{--}1.68 \times 10^{-8} \text{ s}^{-1}$ respectively during five cycles. The measure-


Table 1 | The parameter and thermal barrier ΔE_a of Z \rightarrow E thermal reversion

	Kinetics Constant (k)	Half-life ($\tau_{1/2}$)	ΔE_a
<i>Para</i> -AZO	0.295 s^{-1}	2.35 s	0.79 eV
RGO- <i>para</i> -AZO	$1.66 \times 10^{-6} \text{ s}^{-1}$	116 h	1.1 eV
<i>Ortho</i> -AZO	$1.60 \times 10^{-6} \text{ s}^{-1}$	120 h	1.1 eV
RGO- <i>ortho</i> -AZO	$3.56 \times 10^{-8} \text{ s}^{-1}$	5408 h	1.2 eV

ment of κ_{rev} of RGO-*ortho*-AZO is based on the kinetics of thermal reversion before $\tau_{1/2}$ (5408 h). This feature indicates a good photostability of *ortho*-AZO and *para*-AZO on RGO. Good cycling stability of reversible isomerization-reversion is important for solar thermal storage.

The capacity of solar thermal storage is another key performance parameter for the utilization. The theoretical capacity of thermal energy of RGO-AZO hybrids is calculated using the PAW formalism of spin polarized DFT based on ΔH for per AZO molecule and packing density. The relaxed steric structures of Z- and E-isomers of RGO-*para*-AZO and RGO-*ortho*-AZO hybrids were shown in the inset of Figure 6, in which green and brown dash line indicate inter- and intramolecular H-bonds, respectively. The model is that one AZO molecule is supported by 16 carbon atoms of RGO. The ΔH , packing density (the weight percentage of AZO for RGO-AZO according to TGA and XPS results in experiment) and energy density (thermal energy stored by a quantity of RGO-AZO) are shown in Table 2. Compared with pure AZO molecules (*para*-AZO: 0.558 eV, *ortho*-AZO: 0.77 eV), one-fold increase in ΔH for per AZO molecule is obtained due to the increased energy level between Z- and E-isomers by the formation of intermolecular H-bonds between two adjacent AZO molecules on RGO according to stable configurations (dash line Figure S8).

The different numbers of H-bonds between *ortho*-AZO and *para*-AZO on RGO are indicated by high ΔE_a (1.2 eV) of RGO-*ortho*-AZO controlled by intramolecular H-bonds in Z-*ortho*-AZO and high ΔH (1.38 eV) of RGO-*para*-AZO controlled by one intermolecular H-bond in E-*para*-AZO¹³. This analysis is also confirmed by relaxed steric structures of RGO-*para*-AZO and RGO-*ortho*-AZO hybrids. As shown in Table 2, RGO-*para*-AZO hybrid shows a higher ΔH of 1.38 eV than that of RGO-*ortho*-AZO (1.224 eV). This feature indicates that ΔH for per AZO on RGO is controlled by the number of intra- and intermolecular H-bonds formed in both Z- and E-isomers on RGO. Previous calculation demonstrated that

Table 2 | ΔH , packing density and energy density of thermal storage based on experimental measurement and calculation

	ΔH (eV)	Packing Density (wt%)	Energy Density (kJ/kg)	
			Calculation	Experiment
<i>Para</i> -AZO	0.558		217.9	/
RGO- <i>para</i> -AZO	1.38	57.9	372.2	269.8
<i>Ortho</i> -AZO	0.77		282.4	/
RGO- <i>ortho</i> -AZO	1.224	60.6	274.9	149.6 ^[a]

^[a]The thermal energy were measured until the half-lives of thermal reversion of Z-isomers.

maximizing the number of H-bonds in E-AZO and minimizing H-bonds in Z-AZO provided a high ΔH ¹³. As shown in Figure S8, there is one intermolecular H-bond of =S-OH---OH-S= in E-*para*-AZO (confirmed by red-shifted bands in Figure 3a) and no H-bonds in Z-*para*-AZO on RGO, while both Z-*ortho*-AZO and E-*ortho*-AZO on RGO show one intramolecular H-bond of =N---HO (confirmed by large chemical shift at 13.85) and one intermolecular H-bond of =S-OH---OH-S= (confirmed by red-shifted bands in Figure 3d). Intramolecular H-bonds of RGO-*ortho*-AZO are also indicated by high ΔE_a . E-*para*-AZO and Z-*para*-AZO on RGO exhibit a larger difference in number of H-bonds than that of RGO-*ortho*-AZO. Results suggest that RGO-*para*-AZO with only one intermolecular H-bond results in a high ΔH but a low ΔE_a . In contrast, intramolecular H-bonds in Z-*ortho*-AZO on RGO increase ΔE_a , but multiple (intra- and intermolecular) H-bonds in both Z- and E-*ortho*-AZO lead to a low ΔH . Table 2 display that compared with RGO-*para*-AZO, the increase in ΔE_a by 9% ($\tau_{1/2}$ up to ~ 5000 h) of RGO-*ortho*-AZO is gained at the sacrifice of the decrease in ΔH by 11%. This feature suggests that ΔH and ΔE_a are determined by different molecular H-bonds of Z- and E-AZO controlled by the substitution and microstructures on RGO. Thus, maximizing both ΔH and ΔE_a by optimizing intra- and intermolecular H-bonds of AZO bound on graphene still needs more deep studies in the future.

The amount of heat released by RGO-AZO solution during Z \rightarrow E reversion determined by ΔH for per AZO on RGO was measured using a three-dimensional high-precision calorimetric sensor in a sealed insulating vessel. The solution was completely sealed by thick walls to keep the constant temperature at 19–20°C during the measurement. The densities of heat (related to the capacity of thermal energy stored by a quantity of RGO-AZO) released by (a) RGO-*para*-AZO and (b) RGO-*ortho*-AZO hybrids with the time in darkness after the irradiation are shown in Figure 6. Curves follow three-order fitting exponential decay (Table S3).

The density of heat released by RGO-*para*-AZO hybrids is 269.8 kJ kg⁻¹ when hybrids are kept in a sealed dark vessel after the irradiation for 600 h, which is the time required for almost complete reversion (>95 wt.% Z-*para*-AZO transforms to E-*para*-AZO) calculated based on the change in absorption intensity (Figure 5). Meanwhile, compared with RGO-*para*-AZO, RGO-*ortho*-AZO shows a relative low density of 149.6 kJ kg⁻¹ when hybrids are kept for 5400 h, which is only $\tau_{1/2}$ for Z-*ortho*-AZO on RGO. Thus, this density might be 50% capacity of energy stored by hybrids. It's definitely difficult to measure the maximum capacity of heat storage for RGO-*ortho*-AZO hybrid because of a very long time of complete reversion up to 23333 hours (972 days, according to κ_{rev} in Table 2). The measurement might be disturbed by the environmental temperature. Despite that, the densities of thermal storage of RGO-AZO hybrids are better than that of azo-polymers and derivatives reported recently due to the formation of intra- and intermolecular H-bonds in RGO-AZO^{5,25}. As shown in Table 2, the densities of heat released by RGO-AZO hybrids in experiment are of the same order magnitude to that (RGO-*para*-AZO: 312.2 kJ kg⁻¹ and RGO-*ortho*-AZO: 274.9 kJ kg⁻¹) based on ΔH calculated by DFT and

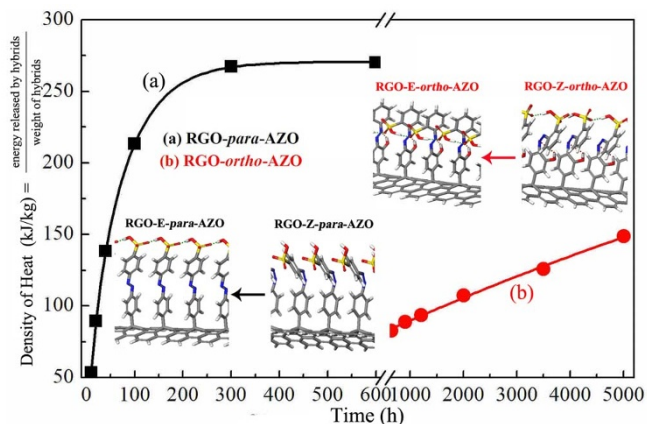


Figure 6 | The density of heat released by (a) RGO-*para*-AZO and (b) RGO-*ortho*-AZO hybrids with the time of storage in darkness (a sealed vessel) after the irradiation and inset shows the stable structures of RGO-AZO hybrids based on the calculated by DFT. White, gray, blue, red and yellow sticks represent H, C, N, O and S atoms, respectively.



packing density. Besides, the volumetric density of thermal storage for RGO-*para*-AZO and RGO-*ortho*-AZO hybrid is about 180 and 100 Wh/L.

Conclusion. *Para*-AZO and *ortho*-AZO bound on RGO with different molecular H-bonds controlled by the substitution and high packing density were presented for solar thermal storage. The covalent attachment showed that per AZO molecule was supported by 11–12 carbon atoms of RGO according to the characterization of chemical structures and thermal stability. Intra- and Intermolecular H-bonds in RGO-AZO hybrid were confirmed by large chemical shifts in ^1H NMR, red-shifted band in FT-IR, and relaxed structures calculated by DFT, leading to the increase in ΔE_a and ΔH for per AZO on RGO, respectively. Intramolecular H-bonds thermally stabilized *Z-ortho*-AZO on RGO with a long-term $\tau_{1/2}$ of 5400 h ($\Delta E_a = 1.2$ eV), which was much longer than that of RGO-*para*-AZO (116 h). RGO-*para*-AZO with one intermolecular H-bond showed high density of thermal storage up to 269.8 kJ kg $^{-1}$ compared with RGO-*ortho*-AZO (149.6 kJ kg $^{-1}$) with multiple intra- and intermolecular H-bonds in both *Z*- and *E*-AZO. Thermal storage in experiment are of the same order magnitude to that (RGO-*para*-AZO: 312.2 kJ kg $^{-1}$ and RGO-*ortho*-AZO: 274.9 kJ kg $^{-1}$) calculated based on ΔH calculated by DFT and packing density. Results indicated that ΔH and ΔE_a are determined by different molecular H-bonds of *Z*- and *E*-AZO on RGO. Thus, optimizing intra- and intermolecular H-bonds of both *Z*-AZO and *E*-AZO bound on graphene is critical for maximizing both ΔH and ΔE_a . RGO-AZO hybrid with the density of 150 ~ 300 kJ kg $^{-1}$ and half-lives of 1000–5000 h can be utilized for a long-term and renewable solar thermal storage.

Methods

Materials. Graphite was obtained from Qingdao Huarun graphite Co. Ltd., with a particle size of 20 μm . *Para*-AZO and all other chemicals were bought from Sigma-Aldrich and used as received.

Synthesis of RGO Single-layer. GO was prepared through acid oxidation of flake graphite. GO were dispersed and partially reduced in 30 mL of NaBH $_4$ solution (pH = 9) at 80°C for 1 h. RGO was obtained after rinsing with di-water, the filtration and the centrifugation at 500 rpm for 10 min.

Synthesis of *ortho*-AZO. Orthanilic acid (18 mmol), NaOH (18 mmol) and NaNO $_2$ (20 mmol) were dissolved in 120 mL of di-water, and the solution was slowly added into 70 mL of HCl (1 mol/L) in an ice bath at 0–5°C for the diazotization. *m*-Aminophenol (18 mmol) was dissolved in 40 mL of HCl. The diazotized compounds were added into *m*-aminophenol solution (pH = 5–7) at 0–5°C for 2 hours. The resultant raw materials were re-crystallized by EtOH-H $_2$ O (1 : 1) for several times, and *ortho*-AZO (14 mmol, Yield: 78%) was collected after washing with di-water, the filtration and dry in vacuum overnight at 70°C. ^1H NMR (CD $_2$ Cl $_2$, δ): 14.19 (s, 1H, Ar-OH), 5.39 (s, 2H, Ar-NH $_2$), 7.84 (d, $J = 8.2$ Hz, 1H, Ar-H), 7.74 (dd, $J = 7.7$, 1.5 Hz, 1H, Ar-H), 7.49 (td, $J = 7.7$ Hz, 1.5 Hz, 1H, Ar-H), 7.45 (d, $J = 9.3$ Hz, 1H, Ar-H), 7.27 (td, $J = 7.7$ Hz, 1.5 Hz, 1H, Ar-H), 6.61 (dd, $J = 9.3$, 1.8 Hz, 1H, Ar-H), 6.21 (d, $J = 2$ Hz, 1H, Ar-H).

Synthesis of RGO-AZO hybrid. AZO molecules were covalently functionalized with RGO by the diazotization using diazonium salts. RGO was dispersed in water to form a homogeneous solution by ultrasonication for 2 hours. The aggregate was removed after the centrifugation at 1000 rpm for 20 min, yielding a typical concentration of 1 mg/mL RGO solution (150 mg). *Ortho*-AZO (6 mmol), NaOH (6 mmol) and NaNO $_2$ (7 mmol) were dissolved in 40 mL of di-water at room temperature, and then the mixture was slowly added to a 40 mL of HCl (1 mol/L) solution in an ice bath and it formed a diazotized salt in one hour. This diazotized salt of AZO (0.075 mmol/mL) was dripped into the above RGO solution. The reaction was carried out for 4 hours at 0–5°C and at room temperature for another 6 hours. The mixture was diluted by 150 mL of acetone and filtered using polytetrafluoroethylene (Teflon) membrane. The compounds were repeatedly washed with di-water to remove excess diazonium salts by the filtration and the centrifugation. RGO-*ortho*-AZO was obtained after dry in vacuum overnight at 70°C with a yield of 125 mg. RGO-*para*-AZO hybrid was prepared by the similar diazotization for the comparison.

Characterization. FT-IR spectra were recorded on a Bruker Tensor 27 spectrometer with a disc of KBr. ^1H NMR spectra of *ortho*-AZO and RGO-*ortho*-AZO were carried out on a Varian INOVA 500 MHz spectrometer with trimethylsilyl as an internal standard. X-ray (1250 eV) source at a base pressure in the 10 $^{-8}$ to 10 $^{-9}$ Torr range. X-

ray diffraction (XRD) patterns were taken by a Rigaku D/max 2500 v/pc X-ray diffractometer using Cu K α radiation ($k = 0.15$ nm) at a scanning rate of 8.0°/min, using a voltage of 40 kV and a current of 200 mA. Thermal analysis was studied using a Thermogravimetric Analyzer Instrument (NETZSCH STA 449C). The samples were heated from 30°C to 700°C at a rate of 5°C/min in an aluminum crucible under 50 mL/min of nitrogen purging. XPS analyses were performed on a PHI 1600 model surface analysis system with a 450 W MgK α . TEM (Philips Tecnai G 2 F20 at 200 kV) and scanning electronic microscope (SEM, Hitachi S-4800) were both performed to observe the morphologies. The surface of GO was observed by AFM (Veeco Multimode III).

Time-evolved UV-vis absorption spectra of AZO and RGO-AZO hybrids in dimethylformamide (DMF) solution using 1 cm pathlength quartz cuvettes were recorded using a Hitachi 330 UV-vis spectrophotometer. *E* \rightarrow *Z* isomerization of RGO-*para*-AZO and RGO-*ortho*-AZO were irradiated by mercury lamp (Beijing Changtuo Technology Company) at 500 W with a filter set of 365 nm and 435 nm respectively, as a light source positioned at 50 cm distance to the samples at room temperature. *Z* \rightarrow *E* thermal reversion of solution was investigated using UV-vis spectrophotometer after the storage in darkness covered by foils. First-order rate constants of reversion at room temperature were calculated based on the change in intensity of transition bands of AZO on RGO.

RGO-*para*-AZO and RGO-*ortho*-AZO hybrids in DMF solutions were irradiated by mercury lamp (Beijing Changtuo Technology Company) at 500 W with a filter set of 365 nm and 435 nm at room temperature, and then 50 mL solution (0.8 mg/mL) were moved in a sealed insulating vessel at the vacuum of 10 $^{-3}$ MPa. The release of heat by *Z* \rightarrow *E* thermal reversion was measured using a three-dimensional high-precision Pt microcalorimetric sensor at room temperature (Sataram Instrument). The solution was completely sealed by thick walls to keep the constant temperature at 18–20°C during the measurement. The data was obtained by balancing the reference RGO.

Our total energy and electronic structure calculations were performed using projector augmented wave (PAW) formalism of spin polarized DFT as implemented in the Vienna *ab initio* Simulation Package (VASP)³⁴. An energy cutoff of 450 eV for plane-wave expansion of the PAW's was used. The exchange-correlation functional was approximated with the generalized gradient approximation proposed by Perdew, Burke, and Ernzerhof (PBE)³⁵. The supercell of graphene nano-ribbons containing 32 carbon atoms was used and separated by a vacuum region of more than 15 Å along the *y*-axis and 30 Å along the *x*-axis. The Brillouin zone was sampled using a 1 \times 1 \times 3 Γ -centered *k*-point grid. For all geometry optimizations, we allowed all the internal coordinates relaxed until the Hellmann-Feynman forces are less than 0.01 eV/Å.

1. Armaroli, N. & Balzani, V. The future of energy supply: challenges and opportunities. *Angew. Chem. Int. Ed.* **46**, 52–66 (2007).
2. Kucharski, T. J., Tian, Y. C., Akbulatov, S. & Boulatov, R. Chemical solutions for the closed-cycle storage of solar energy. *Energ. Environ. Sci.* **4**, 4449–4472 (2011).
3. Gur, I., Sawyer, K. & Prasher, R. Searching for a Better Thermal Battery. *Science* **335**, 1454–1455 (2012).
4. Cho, J. *et al.* Single-Molecule-Resolved Structural Changes Induced by Temperature and Light in Surface-Bound Organometallic Molecules Designed for Energy Storage. *ACS Nano* **5**, 3701–3706 (2011).
5. Taoda, H., Hayakawa, K., Kawase, K. & Yamakita, H. Photochemical Conversion And Storage Of Solar Energy By Azobenzene. *J. Chem. Eng. Jpn.* **20**, 265–270 (1987).
6. Pouliquen, J. *et al.* Photoisomerization of *N,N'*-disubstituted indigos. A search for energy storage. *Can. J. Chem.* **62**, 2478–2486 (1984).
7. Yang, Y., Hughes, R. P. & Aprahamian, I. Visible Light Switching of a BF $_2$ -Coordinated Azo Compound. *J. Am. Chem. Soc.* **134**, 15221–15225 (2012).
8. Siewertsen, R. *et al.* Highly Efficient Reversible *Z* \rightarrow *E* Photoisomerization of a Bridged Azobenzene with Visible Light through Resolved S1($\pi\pi^*$) Absorption Bands. *J. Am. Chem. Soc.* **131**, 15594–15595 (2009).
9. Takaishi, K. & Kawamoto, M. Synthesis and conformation of substituted chiral binaphthyl-azobenzene cyclic dyads with chiroptical switching capabilities. *Molecules* **16**, 1603–1624 (2011).
10. Beharry, A. A., Sadovski, O. & Woolley, G. A. Azobenzenes photoswitching without ultraviolet light. *J. Am. Chem. Soc.* **133**, 19684–19687 (2011).
11. Bleger, D., Schwarz, J., Brouwer, A. M. & Hecht, S. *o*-Fluoroazobenzenes as readily synthesized photoswitches offering nearly quantitative two-way isomerization with visible light. *J. Am. Chem. Soc.* **134**, 20597–20601 (2012).
12. Dokic, J. *et al.* Quantum chemical investigation of thermal *Z*-to-*E* isomerization of azobenzene derivatives: substituent effects, solvent effects, and comparison to experimental data. *J. Phys. Chem. A* **113**, 6763–6773 (2009).
13. Kolpak, A. M. & Grossman, J. C. Azobenzene-functionalized carbon nanotubes as high-energy density solar thermal fuels. *Nano Lett.* **11**, 3156–3162 (2011).
14. Kolpak, A. M. & Grossman, J. C. Hybrid chromophore/template nanostructures: A customizable platform material for solar energy storage and conversion. *J. Chem. Phys.* **138**, 034303 (2013).
15. Feng, W., Luo, W. & Feng, Y. Y. Photo-responsive carbon nanomaterials functionalized by azobenzene moieties: structures, properties and application. *Nanoscale* **4**, 6118–6134 (2012).
16. Peimyoo, N. *et al.* Photocontrolled molecular structural transition and doping in graphene. *ACS Nano* **6**, 8878–8886 (2012).



17. Shashikala, H. B. M., Nicolas, C. I. & Wang, X. Q. Tunable Doping in Graphene by Light-Switchable Molecules. *J. Phys. Chem. C* **116**, 26102–26105 (2012).
18. Lomeda, J. R., Doyle, C. D., Kosynkin, D. V., Hwang, W. F. & Tour, J. M. Diazonium functionalization of surfactant-wrapped chemically converted graphene sheets. *J. Am. Chem. Soc.* **130**, 16201–16206 (2008).
19. Zhu, Y., Higginbotham, A. L. & Tour, J. M. Covalent Functionalization of Surfactant-Wrapped Graphene Nanoribbons. *Chem. Mater.* **21**, 5284–5291 (2009).
20. Englert, J. M. *et al.* Covalent bulk functionalization of graphene. *Nat. Chem.* **3**, 279–286 (2011).
21. An, X. H. *et al.* Stable aqueous dispersions of noncovalently functionalized graphene from graphite and their multifunctional high-performance applications. *Nano Lett.* **10**, 4295–4301 (2010).
22. Sharma, L., Matsuoka, T., Kimura, T. & Matsuda, H. Investigation into the surface relief grating mechanism via XPS in new azobenzene based optical material. *Polym. Adv. Technol.* **13**, 481–486 (2002).
23. Langner, R. & Zundel, G. FT-IR Investigation of Polarizable, Strong Hydrogen Bonds in Sulfonic Acid Sulfoxide, Phosphine Oxide, and Arsine Oxide Complexes in the Middle- and Far-Infrared Region. *J. Phys. Chem.* **99**, 12214–12219 (1995).
24. Zhang, B. W. *et al.* Preparation of polymer decorated graphene oxide by γ -ray induced graft polymerization. *Nanoscale* **4**, 1742–1748 (2012).
25. Yu, D. S., Kulia, T., Kim, N. H., Khanra, P. & Lee, J. H. Effects of covalent surface modifications on the electrical and electrochemical properties of graphene using sodium 4-aminoazobenzene-4'-sulfonate. *Carbon* **54**, 310–322 (2013).
26. Fang, M., Wang, K. G., Lu, H. B., Yang, Y. L. & Nutt, S. Covalent polymer functionalization of graphene nanosheets and mechanical properties of composites. *J. Mater. Chem.* **19**, 7098–7105 (2009).
27. Zhu, Y., James, D. K. & Tour, J. M. New Routes to Graphene, Graphene Oxide and Their Related Applications. *Adv. Mater.* **24**, 4924–4955 (2012).
28. Yang, Y. M., Tang, B. T. & Zhang, F. Light-thermal conversion organic shape-stabilized phase-change materials with broadband harvesting for visible light of solar radiation. *RSC Adv.* **2**, 11372–11378 (2012).
29. Robertus, J. *et al.* Kinetic analysis of the thermal isomerisation pathways in an asymmetric double azobenzene switch. *Phys. Chem. Chem. Phys.* **14**, 4374–4382 (2012).
30. Bandara, H. M. D. & Burdette, S. C. Photoisomerization in different classes of azobenzene. *Chem. Soc. Rev.* **41**, 1809–1825 (2012).
31. Bandara, H. M. D. *et al.* Proof for the concerted inversion mechanism in the trans \rightarrow cis isomerization of azobenzene using hydrogen bonding to induce isomer locking. *J. Org. Chem.* **75**, 4817–4827 (2010).
32. Emond, M. *et al.* 2-Hydroxyazobenzenes to tailor pH pulses and oscillations with light. *Chem. Eur. J.* **16**, 8822–8831 (2010).
33. Gao, J. *et al.* Azobenzene-containing supramolecular polymer films for laser-induced surface relief gratings. *Chem. Mater.* **19**, 14–17 (2007).
34. Kresse, G. & Joubert, D. From ultrasoft pseudopotentials to the projector augmented-wave method. *Phys. Rev. B* **59**, 1758–1775 (1999).
35. Perdew, J. P., Burke, K. & Erzerhof, M. Generalized Gradient Approximation Made Simple. *Phys. Rev. Lett.* **77**, 3865–3868 (1996).

Acknowledgments

This work was financially supported by the National Basic Research Program of China (Grant no. 2012CB626800), the National Natural Science Foundation of China (Grant no. 51003072, 51173127, 51273144 and 51373116), and the Research Fund for the Doctoral Program of Higher Education of China (Grant no. 20110032110067).

Author contributions

F.Y.Y. and F.W. conceived the project and designed the research. L.H.P. and L.W. performed the experiment and characterization. L.E.Z. and Z.N.Q. performed the calculation. Y.K. helped the analysis of the result. All authors reviewed the manuscript.

Additional information

Supplementary information accompanies this paper at <http://www.nature.com/scientificreports>

Competing financial interests: The authors declare no competing financial interests.

How to cite this article: Feng, Y.Y. *et al.* Covalent functionalization of graphene by azobenzene with molecular hydrogen bonds for long-term solar thermal storage. *Sci. Rep.* **3**, 3260; DOI:10.1038/srep03260 (2013).



This work is licensed under a Creative Commons Attribution-NonCommercial-NoDerivs 3.0 Unported license. To view a copy of this license, visit <http://creativecommons.org/licenses/by-nc-nd/3.0>